High-resolution simulation of pattern formation and coarsening dynamics in 3D convective mixing

by

Xiaojing Fu

Submitted to the School of Engineering
in partial fulfillment of the requirements for the degree of

Master of Science in Computation Design and Optimization

at the

MASSACHUSETTS INSTITUTE OF TECHNOLOGY

June 2015

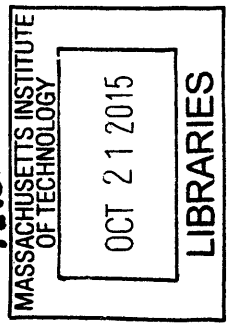

Author .. Signature redacted .....
School of Engineering
June, 2015

Certified by Signature redacted .....
Ruben Juanes
Associate Professor of Civil and Environmental Engineering
Thesis Supervisor

Accepted by Signature redacted .....
Nicolas Hadjiconstantinou
Co-director, Computation Design and Optimization

High-resolution simulation of pattern formation and coarsening dynamics in 3D convective mixing

by

Xiaojing Fu

Submitted to the School of Engineering
on June, 2015, in partial fulfillment of the
requirements for the degree of
Master of Science in Computation Design and Optimization

Abstract

Geologic CO_2 sequestration is considered a promising tool to reduce anthropogenic CO_2 emissions while allowing continued use of fossil fuels for the current time. The process entails capturing CO_2 at point sources such as coal-fired power plants, and injecting it in its supercritical state into deep saline aquifers for long-term storage. Upon injection, CO_2 partially dissolves in groundwater to form an aqueous solution that is denser than groundwater. The local increase in density triggers a gravitational instability at the boundary layer that further develops into columnar CO_2-rich plumes that sink away. This mechanism, also known as convective mixing, greatly accelerates the dissolution rate of CO_2 into water and provides secure storage of CO_2 underground. Understanding convective mixing in the context of CO_2 sequestration is essential for the design of injection and monitoring strategies that prevent leakage of CO_2 back into the atmosphere. While current studies have elucidated various aspects of this phenomenon in 2D, little is known about this process in 3D.

In this thesis we investigate the pattern-formation aspects of convective mixing during geological CO_2 sequestration by means of high-resolution three-dimensional simulation. We find that the CO_2 concentration field self-organizes as a cellular network structure in the diffusive boundary layer right beneath the top boundary. By studying the statistics of the cellular network, we identify various regimes of finger coarsening over time, the existence of a nonequilibrium stationary state, and an universal scaling of 3D convective mixing. We explore the correlation between the observed network pattern and the 3D flow structure predicted by hydrodynamics stability theory.

Thesis Supervisor: Ruben Juanes
Title: Associate Professor of Civil and Environmental Engineering

Acknowledgments

I would like to express my deepest gratitude to my research advisor, Ruben Juanes, for your insightful teaching, encouragement, wisdom and patience;

To my dearest collaborator and mentor Luis Cueto-Felgueroso, I am deeply grateful for your unreserved sharing of knowledge, your wisdom, patience and friendship;

I owe my achievement to the full-hearted support from the members of the Juanes Research Group and the Parsons laboratory, with you I share great memories;

To the administrative staff at the CDO program, Barbara Lechner, thank you for being so strong for yourself and so supportive to the CDO students during your years with us; we miss you deeply;

and, last but not least, to my parents Ming Fu and Li Wan, and my partner Ryan Lewis for your love, encouragement and companion. I am so blessed to have you in my life.

Contents

1 Introduction **13**

2 High-resolution simulation of 3D convective mixing **15**

2.1 Convective mixing model 15

2.2 Scaling analysis 16

2.3 The stream-function-vorticity formulation 17

2.4 Numerical implementation and visualization 19

3 Pattern formation and coarsening dynamics **21**

3.1 Pattern formation at the top boundary 21

3.2 Coarsening dynamics 25

3.3 Universality of coarsening dynamics 30

4 Flow structure and pattern forming mechanisms **33**

4.1 Rayleigh-Bénard convection and linear stability analysis 33

4.2 Linear stability analysis 35

4.3 Analytical and simulated two-dimensional cell patterns 39

5 Conclusion **43**

List of Figures

3-1 Simulation of convective mixing with Ra = 6400 on a 512^3 grid. (a) Snapshot of the concentration field at a slice near the top boundary ($z = 0.01$) at $t = 0.5$, showing a pattern of disconnected islands of high concentration. (b) Snapshot of the same slice at $t = 1$, showing a partially-connected maze structure. (c)-(e) Snapshot of the 3D concentration field at $t = 2$; (c) is a complete view of the computational domain; (d) is a view of a partial volume ($0.01 < z < 0.3$) from the top, illustrating the cellular network structure that emerges at the boundary layer; (e) is a view of the same volume from the bottom, illustrating the columnar pattern of CO_2-rich fingers that sink away from the top boundary. 22

3-2 Concentration field at $t = 10$ for the 3D simulation with Ra=6400, at different depths. (a) $z = 0.001$, (b) $z = 0.04$, (c) $z = 0.12$, and (d) $z = 0.43$. 24

3-3 (a) Snapshot of the velocity field at a depth $z = 0.01$ at time $t = 13$ for Ra = 6400, showing upward flow at the cell centers (grayscale) and downward flow at the cell edges (white), and horizontal flow from the center to the edges of individual cells (red arrows). (b) Zoomed view of a small area of the same slice (blue square) at different times, illustrating cell growth and disappearance of small cells ($t = 11.6$ to $t = 11.7$), and cell division from the emergence of sheets of high concentration within cells ($t = 11.7$ to $t = 11.8$). 26

3-4 Evolution of the power spectrum density for the concentration field of a horizontal slice ($z = 0.01$) of the simulation with Ra $= 6400$. The onset wave number inferred from the numerical simulations is $k \approx 40$, corresponding to the maximum energy content for the solution at $t = 0.2$. While this number should be understood as a plausible range rather than a hard value, it does agree nicely with the result of a linear stability analysis (as extrapolated from Fig. 11 in [29]). . . . 27

3-5 (a) Snapshot of the concentration field at $t = 10$, $z \approx 0.01$ for a 3D simulation with Ra=6400. (b) The dark lines mark the binary skeleton representation of the same network shown in (a). The red circles are the network joints identified by image processing tool. (c) Snapshot of the concentration field near the top boundary of a 2D simulation with Ra=10000 at $t = 10$. The black dotted line indicates $z \approx 0.005$, the depth at which we extract the 1D concentration. (d) The black solid line is the 1D concentration signal obtained from (c); the red circles are the peaks identified by the peak-finding tool. 28

3-6 Time evolution of cell size (l_{cell}) in 3D simulations for different Rayleigh numbers. The two dashed lines indicate the time averaging window ($10 < t < 15$) used to calculate the characteristic cell length during the nonequilibrium steady state regime of the network. 29

3-7 Time evolution of non-dimensional flux (blue) and cell length near the boundary (green). (a) 3D simulation with Ra=6400. (b) 2D simulation with Ra=25,000. 29

3-8 Characteristic length $\bar{l}$ plotted against Rayleigh number. (a) 3D simulations; (b) 2D simulations. This characteristic length scale exhibits a power-law dependence with Rayleigh number $\bar{l} \sim \text{Ra}^{-1}$. 31

4-1 A simplified diagram of the Bénard experiment and illustration of the convection cells in vertical direction. 34

4-2 Image from [17]. The following captions are from [38]: "Imperfections in a hexagonal Bénard convection pattern. The hexagonal pattern of cells typical of convective instability driven primarily by surface tension is seen to accommodate itself to a circular boundary. Aluminum powder shows the flow in a thin layer of silicone oil of kinematic viscosity 0.5 cm^2/s on a uniformly heated copper plate. A tiny dent in the plate causes the imperfection at the left, forming diamond-shaped cells. This shows how sensitive the pattern is to small irregularities." 34

4-3 For a simulation of Ra=3200, snapshots at $t = 12$ of horizontal slices at $z = 0.04$. From left to right: concentration field, flow speed in x-y plane (horizontal speed), flow speed in positive z-direction (downward) and flow speed in negative z-direction (upward). 41

Chapter 1

Introduction

Increasing level of greenhouse gas in the atmosphere such as carbon dioxide (CO_2) has led to climate change at a global scale. A significant portion of greenhouse gas originates from anthropogenic CO_2 emissions. Geologic carbon sequestration refers to the long-term, large-scale capture and storage of anthropogenic CO_2 into deep geologic formations [15]. It has been proposed as a promising technology to reduce CO_2 emissions to the atmosphere and mitigate climate change [18, 25, 36]. The proposed procedure consists of three steps: 1) capture of CO_2 from the flue stream of coal- or gas-fired power plants; 2) compression of CO_2 into its supercritical form; and 3) injection of the supercritical fluid through wells into geological formations like deep saline aquifers. Once it has reached the brine-saturated formation, the initially buoyant CO_2 mixes with groundwater by diffusion and creates an aqueous solution that is denser than the ambient brine. The increase in fluid density results in a configuration that is gravitationally unstable, and results in a Rayleigh–Bénard-type hydrodynamic instability that leads to stronger mixing of fluids as is controlled by both advection and diffusion rather than diffusion alone [39, 20, 6, 29]. This convective mixing phenomenon is often referred to as "solubility trapping" in the context of carbon sequestration as it enhances the dissolution rate of CO_2 into water and allows the initially buoyant gas to be safely dissolved and stored away in groundwater-filled formation.

Gravity-driven convection in porous media has been a subject of extensive study

[see, e.g., 24] and it has recently attracted renewed attention in the context of CO_2 sequestration. After an initial period, the overlying dense layer of CO_2-rich groundwater becomes unstable and develops finger-like plumes that protrude downward into the underlying brine and induce convective flow. Using linear and nonlinear stability analysis, one can predict the onset time of convection and the initial spacing between fingering plumes [7, 29, 27, 34]. These initial plumes continue to grow downward, stripping away the dense fluid from the top and thus allowing more CO_2 to dissolve into the underlying groundwater. The fingering plumes exhibit complex dynamics of vertical growth, lateral merging and rebirthing at the top boundary layer, which can be observed using direct numerical simulations in two dimensions [29, 8, 11, 23] and in three dimensions [27, 26] as well as in bench-scale experiments [16, 23, 1, 33]. Much of the previous work has focused on upscaling the dissolution flux [26, 16, 23, 1, 12] as it concerns the efficiency of solubility trapping for carbon sequestration. However, certain aspects of convective mixing remain poorly understood.

In this work, we focus on the formation of intricate patterns in the diffusive boundary layer as a result of the gravitational instability [26, 33, 32]. We describe the entire evolution of the convective-mixing instability in 3D, and the 2D patterns that emerge at the boundary layer. We identify and characterize several regimes in the evolution of these patterns, and report the emergence of a cellular-network structure. We address fundamental questions on the morphology and dynamics of this pattern: What is the evolution that leads to this pattern morphology? Does this pattern reach a pseudo steady-state characterized by a universal length scale? If so, how does this length scale depend on the system parameters? What are the mechanisms responsible for this nonequilibrium stationary state? Are the coarsening dynamics also universal? Here, we explore these questions using 3D high-resolution simulation of convective mixing in porous media. We provide direct visual illustration as well as quantitative analysis of the pattern-forming process. In addition, we address the dissolution flux in 3D in comparison with past observations from 2D simulations, and explain the origin of the observed cellular morphology.

Chapter 2

High-resolution simulation of 3D convective mixing

2.1 Convective mixing model

The following equations describe the convective dissolution process in a homogeneous porous volume, where gravity points in the positive z-direction:

$$\mathbf{u} = -\frac{K}{\mu}(\nabla P - \rho g \hat{\mathbf{z}}) \tag{2.1}$$

$$\phi \frac{\partial c}{\partial t} = -\mathbf{u} \cdot \nabla c + \phi D \nabla^2 c \tag{2.2}$$

$$\nabla \cdot \mathbf{u} = 0 \tag{2.3}$$

$$\rho = \rho_0 + \Delta \rho c \tag{2.4}$$

Eq.(2.1) is Darcy's law; here, $\hat{\mathbf{z}}$ is the unit vector in the direction of gravity, $\mathbf{u} = (u, v, w)$ is the Darcy velocity, K is the permeability, μ is the viscosity, c is the concentration of dissolved CO_2 normalized by the CO_2 solubility in water, ϕ is the porosity, D is the diffusion coefficient, ρ is the density of mixture and ρ_0 is the density of supercritical CO_2. Eq.(2.2) is the advection-diffusion equation (ADE) that describes the transport of dissolved CO_2 in the system; the velocity field here is divergence-free as imposed by Eq.(2.3) and a linear relation between density and

concentration is assumed, as shown in Eq.(2.4).

In 3D, the simulation domain is chosen as a cube ($\Omega = [0, L]^3$) with the following initial conditions:

$$\mathbf{u}(x, y, z) = 0; \qquad c(x, y, z) = 0.$$

For boundary conditions, we assume periodicity in x, y direction and no-flow in z direction with a prescribed concentration at the top boundary:

$$\begin{aligned} w(x, y, z = 0, t) &= 0; & w(x, y, z = L, t) &= 0; \\ c(x, y, z = 0, t) &= 1; & \frac{\partial c}{\partial z} \mid_{x,y,z=L,t} &= 0 \end{aligned}$$

2.2 Scaling analysis

We express the equations in dimensionless form using L as the length scale and the buoyancy velocity U as the velocity scale. We define the following characteristic scales:

$$\begin{aligned} \rho_c &= \Delta\rho, \\ P_c &= \Delta\rho g L, \\ U &= \frac{K P_c}{\mu L} = \frac{K \Delta\rho g}{\mu}, \\ t_c &= \frac{\phi \mu L}{K \Delta\rho g} \end{aligned}$$

The above scaling relationships lead us to the following dimensionless system describing convective mixing:

$$\nabla \cdot \mathbf{u} = 0, \tag{2.5}$$

$$\mathbf{u} = -(\nabla P' - c\hat{\mathbf{z}}), \tag{2.6}$$

$$\frac{\partial c}{\partial t} = -\mathbf{u} \cdot \nabla c + \frac{1}{\mathrm{Ra}} \nabla^2 c, \tag{2.7}$$

where P' is the adjusted pressure after taking out the hydrostatic part: $P' = (P - \rho_0 g z)/\Delta\rho g L$. The system is controlled by the Rayleigh number, which is the ratio between diffusive and convective time scales, defined as:

$$\mathrm{Ra} = \frac{K\Delta\rho g L}{\phi D \mu} \tag{2.8}$$

In non-dimensional form, the boundary conditions are expressed as:

$$\begin{aligned} &w(x, y, z = 0, t) = 0; \qquad && w(x, y, z = 1, t) = 0; \\ &c(x, y, z = 0, t) = 1; \qquad && \frac{\partial c}{\partial z} \mid_{x,y,z=1,t} = 0 \end{aligned}$$

A critical Rayleigh number, Ra_c, can be defined such that when $\mathrm{Ra}<\mathrm{Ra}_c$, the dissolution process is stable and purely diffusive; when $\mathrm{Ra}>\mathrm{Ra}_c$, flow instabilities develop within the top boundary layer and mass dissolution becomes convective. In this problem, we estimate $\mathrm{Ra}_c = 4\pi^2$, obtained from the analysis on a similar problem where instability is driven by thermal gradient [13].

2.3 The stream-function-vorticity formulation

We combine Eq.(2.5) and Eq.(2.6) to arrive at the pressure equation:

$$\nabla \cdot (-\nabla P' + c\hat{\mathbf{z}}) = 0. \tag{2.9}$$

Eq.(2.9) is an elliptic partial differential equation and can be treated as a Poisson problem with the concentration gradient acting as the source term. The pressure field varies over space and needs to be updated at every time step; meanwhile, solving Eq.(2.9) is computationally expensive especially when there is a need for a high resolution grid. To resolve this bottleneck, a stream-function-vorticity formulation of Eq.(2.9) is often used, which allows for the use of an efficient fast Poisson solver. Below we explain the stream-function-vorticity formulation in detail.

The vorticity is defined as the curl of velocity:

$$\begin{aligned}\omega &= \nabla \times \mathbf{u} \\ &= -\nabla \times (\nabla P - c\nabla \hat{\mathbf{z}}) \\ &= \nabla c \times \nabla \hat{\mathbf{z}} \\ &= \left(\frac{\partial c}{\partial y}\right)\hat{\mathbf{i}} + \left(-\frac{\partial c}{\partial x}\right)\hat{\mathbf{j}}\end{aligned} \tag{2.10}$$

Next we assume that there exists some vector stream function Ψ such that:

$$\mathbf{u} = \nabla \times \Psi, \tag{2.11}$$

where

$$\Psi = \begin{bmatrix} \phi \\ \theta \\ \chi \end{bmatrix}, \quad \mathbf{u} = \begin{bmatrix} u \\ v \\ w \end{bmatrix}.$$

The result of taking the curl of the velocity field using the stream function definition in Eq.(2.11) is equivalent to the vorticity defined in Eq. (2.10):

$$\omega = -\nabla^2 \Psi = \left(\frac{\partial c}{\partial y}\right)\hat{\mathbf{i}} + \left(-\frac{\partial c}{\partial x}\right)\hat{\mathbf{j}}.$$

Thus, we can reformulate the pressure equation into the following system on stream functions:

$$\nabla^2 \phi = -\frac{\partial c}{\partial y}, \qquad \text{BC:} \quad \phi_{z=0,1} \equiv 0 \text{ , periodic in } x, y\text{-direction;} \tag{2.12}$$

$$\nabla^2 \theta = \frac{\partial c}{\partial x}, \qquad \text{BC:} \quad \theta_{z=0,1} \equiv 0 \text{ , periodic in } x, y\text{-direction;} \tag{2.13}$$

$$\nabla^2 \chi = 0, \qquad \text{BC:} \quad \chi_{z=0,1} \equiv 0 \text{ , periodic in } x, y\text{-direction.} \tag{2.14}$$

The solution to the boundary value problem described in Eq.(2.14) is simply $\chi = 0$. Therefore we only need to solve for Eq.(2.12) and Eq.(2.13). The velocity field can

then be obtained by taking the curl of Ψ:

$$u = -\frac{\partial \theta}{\partial z} \tag{2.15}$$

$$v = \frac{\partial \phi}{\partial z} \tag{2.16}$$

$$w = \frac{\partial \theta}{\partial x} - \frac{\partial \phi}{\partial y} \tag{2.17}$$

2.4 Numerical implementation and visualization

The computation can be divided into three parts: a) computing concentration gradients in x, y and z-directions, b) solving for the stream functions in Eq.(2.12) and Eq.(2.13), and c) integrating in time. For the gradient calculation, periodicity in the x- and y-directions allows us to use the computationally-efficient spectral method [37]; in the z-direction we use a sixth-order compact finite difference scheme [19] and make proper adjustment to the differentiation matrix to accommodate the no-flow boundary conditions at the top and bottom of the domain. The stream functions ϕ and θ are computed using the fast Poisson solver [35]. An explicit three-stage Runge-Kutta method [30] is used for time integration. The time step is dynamic and is chosen according to the stability criterion of the numerical scheme.

The initial condition is perturbed with uniformly distributed random noise around the top boundary with a mean value of 1. This technique promotes the instability and shortens the time before fingers form, thus saving computation time.

We conduct 3D simulations with Rayleigh numbers between Ra = 1600 and 6400 using grid resolutions between 128^3 and 512^3 ($N \approx \mathrm{Ra}/13$). Convergence tests ensure that the chosen grid resolutions are sufficient to resolve the corresponding Rayleigh numbers. We perform these simulations on GPUs to reduce computing time and generate 3D visualization of the results in ParaView[9].

Chapter 3

Pattern formation and coarsening dynamics

In this chapter, we discuss observations from simulations of convective mixing with Rayleigh numbers up to 6400 and describe the 3D dynamics of the system along with the 2D pattern forming process at the top boundary layer.

3.1 Pattern formation at the top boundary

The top boundary of the system is initially diffusive and stable; over time, however, the flux of CO_2 at the top ($c = 1$) destabilizes this layer and triggers gravity-driven convection. To reduce the onset time of this Rayleigh-Bénard-type hydrodynamic instability, we perturb the initial condition at the top with random Gaussian white noise. After onset, the diffusive layer exhibits a sequence of 2D patterns:

1. *Islands:* Immediately after onset of instability, the originally flat diffusive dissolution front gives way to downward-moving protrusions, and transforms into a bumpy 3D iso-concentration surface. A 2D view of the concentration field within the boundary layer reflects these bumps in the form of disconnected islands of high-concentration surrounded by zero-concentration brine [Fig. 3-1 (a)]. Our high-resolution simulations clearly illustrate the columnar pattern in

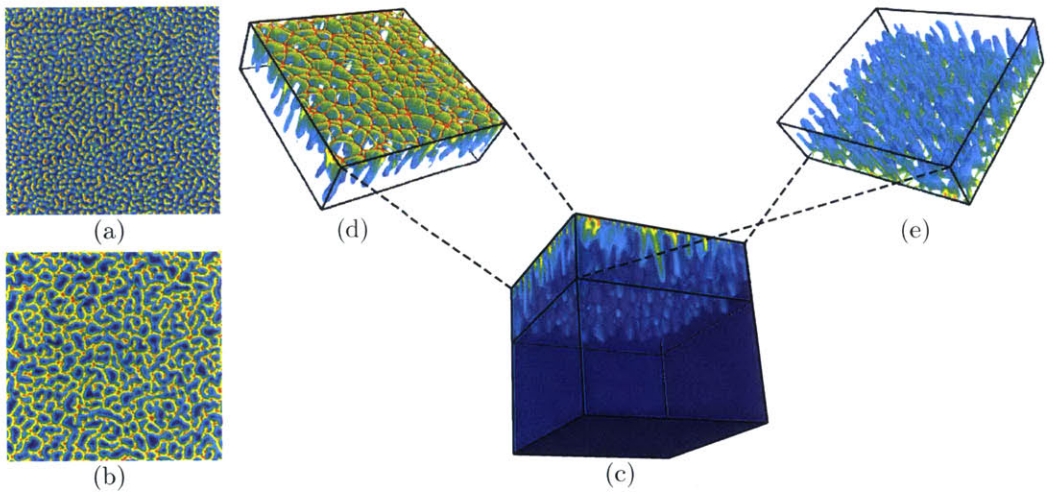

Figure 3-1: Simulation of convective mixing with Ra = 6400 on a 512^3 grid. (a) Snapshot of the concentration field at a slice near the top boundary ($z = 0.01$) at $t = 0.5$, showing a pattern of disconnected islands of high concentration. (b) Snapshot of the same slice at $t = 1$, showing a partially-connected maze structure. (c)-(e) Snapshot of the 3D concentration field at $t = 2$; (c) is a complete view of the computational domain; (d) is a view of a partial volume ($0.01 < z < 0.3$) from the top, illustrating the cellular network structure that emerges at the boundary layer; (e) is a view of the same volume from the bottom, illustrating the columnar pattern of CO_2-rich fingers that sink away from the top boundary.

the onset regime, with a characteristic length that agrees well with predictions from linear stability analysis, $l_{\text{onset}} \sim \text{Ra}^{-1}$ [29].

2. *Maze:* The initially disconnected islands evolve by bridging among themselves and become increasingly connected over time, giving rise to a maze-like morphology in 2D [Fig. 3-1 (b)]. The emergence of this maze structure cannot be anticipated from 2D simulations. Our 3D simulations demonstrate that the bridges between islands form a maze structure that later develops into hexagonal cellular network.

3. *Cellular network:* Continued forcing from the top transforms the maze-like structure in two ways: the thinning of maze walls and reorganization towards a fully connected polygonal network consisting of high-concentration cell boundaries enclosing low-concentration cell interiors [Fig. 3-1 (c)-(d), Fig. 3-2 (a)]. The cell wall thickness is controlled by two mechanisms: lateral diffusion across the cell and downward vertical advection through the wall, similar to the mechanism described for boundary layer thickness [29]. We perform a careful analysis and confirm that both boundary layer and cell wall thickness scale with $\sim \text{Ra}^{-1}$. Beneath the cellular structure, we observe a brief transition into a structure of different nature: a forest of disconnected columnar fingers. The cellular vertices host the maximum downward CO_2 flux, acting as roots for the downward-growing fingers [Fig. 3-1 (c)-(e)]. The dynamics within the cellular network, namely cell zipping and merging in the horizontal plane, are fast compared to the dynamics of downward-migrating columnar fingers. Hence, even though the columnar fingers are continuation of the cellular network atop, the structure of the interior domain is not a direct reflection of the network morphology (Fig. 3-2).

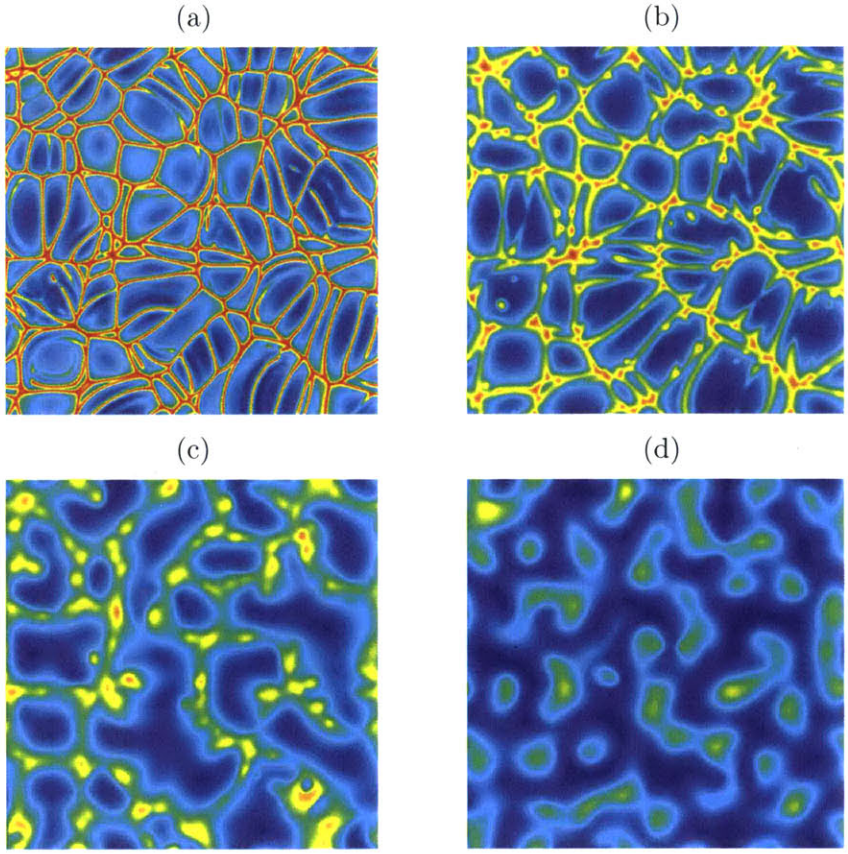

Figure 3-2: Concentration field at $t = 10$ for the 3D simulation with Ra=6400, at different depths. (a) $z = 0.001$, (b) $z = 0.04$, (c) $z = 0.12$, and (d) $z = 0.43$.

3.2 Coarsening dynamics

Once the polygonal network becomes fully established at around $t \approx 2$, we observe that the network coarsens through merging and collapsing of small cells while the fingering plumes migrate downwards. This *early-time coarsening* regime lasts untill $t \approx 8$, when the network stabilizes to a *nonequilibrium steady state*, during which two mechanisms act to balance the characteristic cell size for an extended period of time.

1. *Cell growth.* In this first mechanism, small cells continue to vanish from the network through collapsing and merging, leaving space for expansion of larger cells. Looking at the convection-induced velocity field within the boundary layer provides some hints on the process behind the growth mechanism. In an overlapped image of the concentration field and velocity vector field within the boundary layer (Fig. 3-3), we observe that cell centers coincide with upwelling currents of fresh fluid that impinge onto the boundary layer and diverge laterally towards cell edges. During this process, the fresh upwelling currents become recharged with CO_2 at the boundary and reconvene at the cell edges to carry on the downward transportation of concentrated fluid.

2. *Cell division.* While the upwelling currents drive the growth of large cells, they also prime the birth of new cell edges within these large cells. Most of the newborn cell links, or highly concentrated plume sheets, are immediately swept sideways into existing cell boundaries due to strong upwelling current; however, past a certain cell size, the velocity field within becomes low enough to allow newborn cell edges to persist and evolve into cell boundaries, permanently dividing the hosting cell. [Fig. 3-3 (b)].

The first mechanism promotes large cells in the network and is counterbalanced by the second mechanism that penalizes cells that are too large. These two mechanisms reflect the nonequilibrium nature of the convective mixing process. After a long-enough time ($t \approx 20$), the domain becomes sufficiently saturated with CO_2 and the impact of bottom boundary on the dynamics in the top boundary becomes sig-

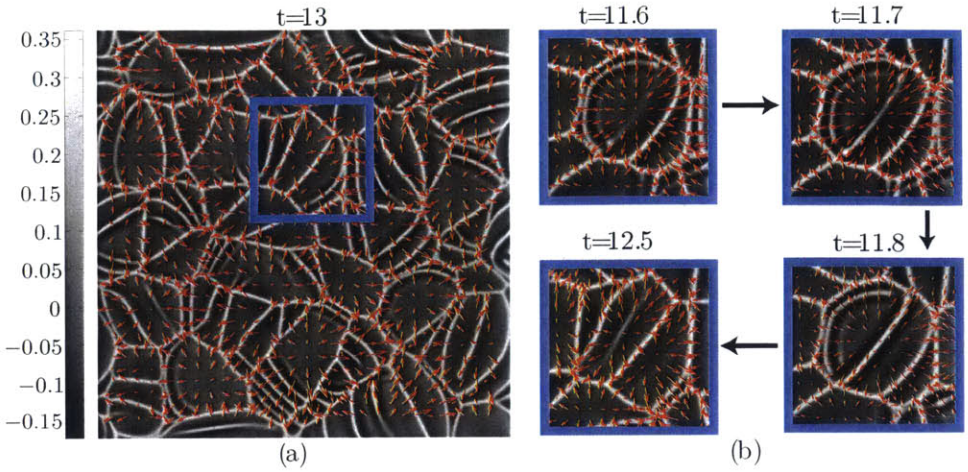

Figure 3-3: (a) Snapshot of the velocity field at a depth $z = 0.01$ at time $t = 13$ for Ra = 6400, showing upward flow at the cell centers (grayscale) and downward flow at the cell edges (white), and horizontal flow from the center to the edges of individual cells (red arrows). (b) Zoomed view of a small area of the same slice (blue square) at different times, illustrating cell growth and disappearance of small cells ($t = 11.6$ to $t = 11.7$), and cell division from the emergence of sheets of high concentration within cells ($t = 11.7$ to $t = 11.8$).

nificant. At this point, the network can no longer sustain its characteristic size and enters a regime of *late-time coarsening* where cell size continues to increase until the disappearance of the network structure.

To demonstrate the existence of the three regimes, we perform a quantitative analysis of the 2D concentration fields within the boundary layer. We compute the power spectrum density ($E(k)$, or PSD) for the concentration field at $z = 0.01$, for a simulation of Ra=6400, at different times [Fig.3-4]. We verify that the network pattern is isotropic by analyzing the 2D Fourier transform of the network images, which indeed exhibit concentric circular isocontours at all times. This allows us to define the 2D wave number as: $k^2 = k_x^2 + k_y^2$, where k_x and k_y are wave numbers in the x- and y- directions, respectively. The wave numbers are also defined in a way such that its corresponding length is calculated as $1/k$ instead of the common form of $2\pi/k$. The power spectrum density is computed as the square of the 2D Fourier transform on the concentration field.

The PSD curves reflect distributions of length scales in the network pattern [Fig.3-4]; the dominant length scale is often marked with the highest $E(k)$. We observe

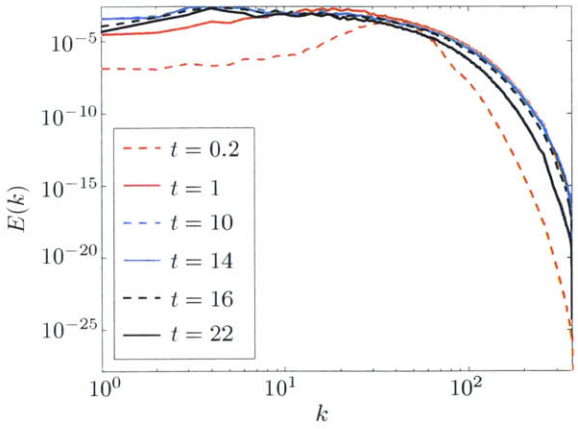

Figure 3-4: Evolution of the power spectrum density for the concentration field of a horizontal slice ($z = 0.01$) of the simulation with Ra = 6400. The onset wave number inferred from the numerical simulations is $k \approx 40$, corresponding to the maximum energy content for the solution at $t = 0.2$. While this number should be understood as a plausible range rather than a hard value, it does agree nicely with the result of a linear stability analysis (as extrapolated from Fig. 11 in [29]).

that during the *early-time coarsening* regime (red curves, corresponding to $t = 0.2$ and $t = 1$), the peak of the spectrum drastically shifts leftward towards smaller k, marking the transitions from *islands* to *maze* and onward to *cellular network*. During *nonequilibrium steady state* (blue curves, corresponding to $t = 10$ and $t = 14$), the spectrum peaks at a smaller k compared to earlier regime, corresponding to an increased length that signifies the average cell diameter; furthermore, the two blue curves overlap almost perfectly, suggesting the statistical steady-state of the pattern. The *late-time coarsening* regime (black curves, corresponding to $t = 16$ and $t = 22$) is signaled by a further left-shift of the curve towards even smaller k, evidencing the continued increase of cell sizes.

We confirm the transitions from an early-time coarsening to a statistical steady state regime by evaluating a representative length scale of the network,

$$l_{\text{cell}} = \frac{1}{\sqrt{N_{\text{fing}}}}, \tag{3.1}$$

where N_{fing} is the number of fingers that root within the network and also corresponds to the number of network joints [Fig.3-5 (a)]. Since there are no statistically significant

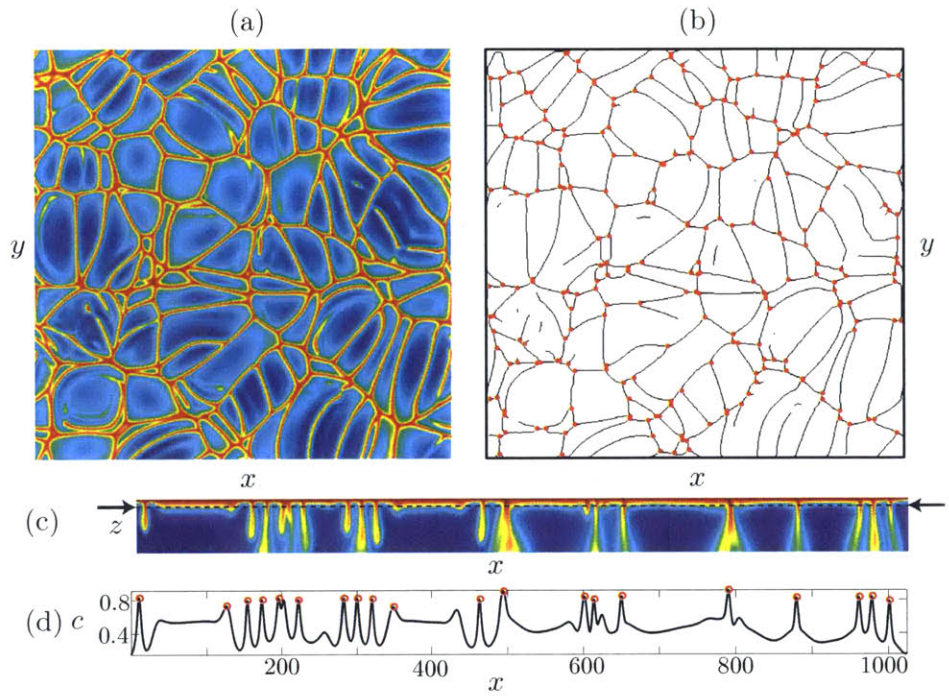

Figure 3-5: (a) Snapshot of the concentration field at $t = 10$, $z \approx 0.01$ for a 3D simulation with Ra=6400. (b) The dark lines mark the binary skeleton representation of the same network shown in (a). The red circles are the network joints identified by image processing tool. (c) Snapshot of the concentration field near the top boundary of a 2D simulation with Ra=10000 at $t = 10$. The black dotted line indicates $z \approx 0.005$, the depth at which we extract the 1D concentration. (d) The black solid line is the 1D concentration signal obtained from (c); the red circles are the peaks identified by the peak-finding tool.

changes in topology during the nonequilibrium steady state, we assume that the number of network joints is linearly related to the number of cells in the network during the steady regime. From observation, we propose to estimate the average cell area $A_{\text{cell}} \sim l_{\text{cell}}^2$ as proportional to the total area of the network (1×1 square) divided by the number of joints (N_{fing}).

A plot of l_{cell} as a function of time illustrates the growth of the characteristic length scale during an initial period ($t < 8$), and a fluctuating, mean-reverting length scale during the quasi-steady period ($8 < t < 20$) (Fig. 3-6). The details of this analysis are discussed in section 3.3 below.

The characteristic length in the system exhibits three dynamic regimes: *early-time coarsening*, *nonequilibrium steady state* and *late-time coarsening*. It is natural

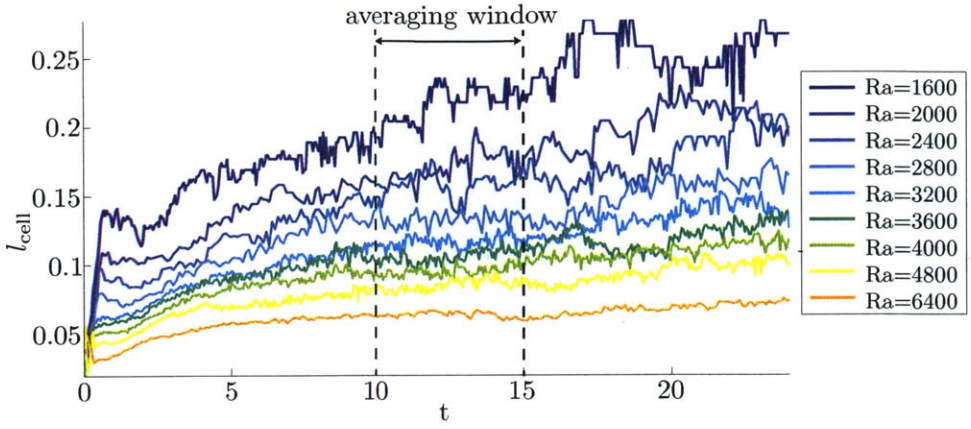

Figure 3-6: Time evolution of cell size (l_{cell}) in 3D simulations for different Rayleigh numbers. The two dashed lines indicate the time averaging window ($10 < t < 15$) used to calculate the characteristic cell length during the nonequilibrium steady state regime of the network.

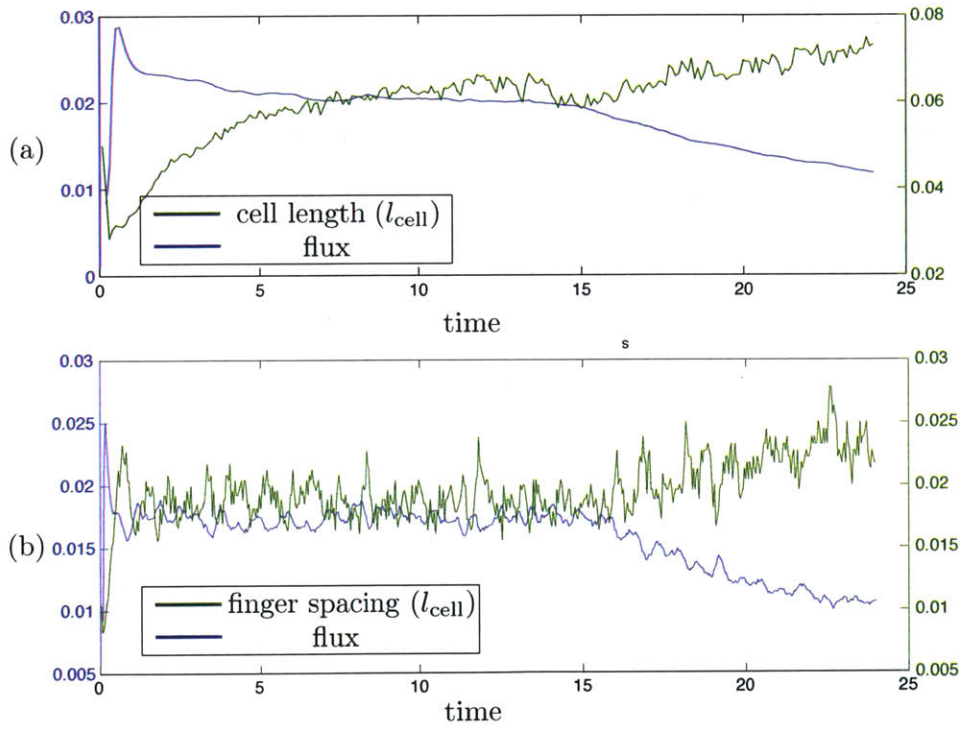

Figure 3-7: Time evolution of non-dimensional flux (blue) and cell length near the boundary (green). (a) 3D simulation with Ra=6400. (b) 2D simulation with Ra=25,000.

to ask whether the coarsening regimes of the length scale near the boundary layer are reflected in the time evolution of dissolution flux. Indeed, the dissolution flux exhibits three dynamic regimes as well: *diffusive*, *convection-dominated* and *saturation* [26, 12, 33, 10]. Here we compare these two quantities—characteristic length scale and dissolution flux—for both a 3D simulation with Ra=6400 and a 2D simulation with Ra=25,000 (Fig. 3-7). The dynamics of these two quantities appear to be highly correlated in time. The magnitude of the dissolution flux, however, is uninformative with respect to the length scale. The nondimensional flux is independent of Ra [12], and clearly this is not the case for the characteristic length scale (Fig. 3-6).

3.3 Universality of coarsening dynamics

The fact that the characteristic length scale of the process reaches a stationary value during an extended period of time raises the question of what sets that length scale. Our hypothesis is that, in the absence of any external length scale in the problem, this characteristic length is set by a balance between advection and diffusion, $l_{\text{diff}} \sim D/U$, where $U = (\Delta\rho g k)/(\phi\mu)$ is the characteristic density-driven fluid velocity. From the definition of the Rayleigh number, Eq. (2.8), we have that $l_{\text{diff}} \sim H/\text{Ra}$. This suggests a linear scaling of cell size with the inverse of Ra,

$$l_{\text{cell}} \sim \text{Ra}^{-1} \tag{3.2}$$

To test this hypothesis, we perform a study of the evolution of cell sizes of the network. We threshold the concentration field to obtain a binary image that can then be reduced to a skeleton representation of the network [Fig. 3-5(b)], using open-source image processing software [31]. We count the number of vertices, or joints, in the skeleton network using a commercially available image processing tool [21], and then estimate the cell length l_{cell} defined in Eq. (3.1).

In Fig. 3-6 we plot the time evolution of l_{cell} for nine different Rayleigh numbers, ranging from 1600 to 6400. We identify the three coarsening regimes described in

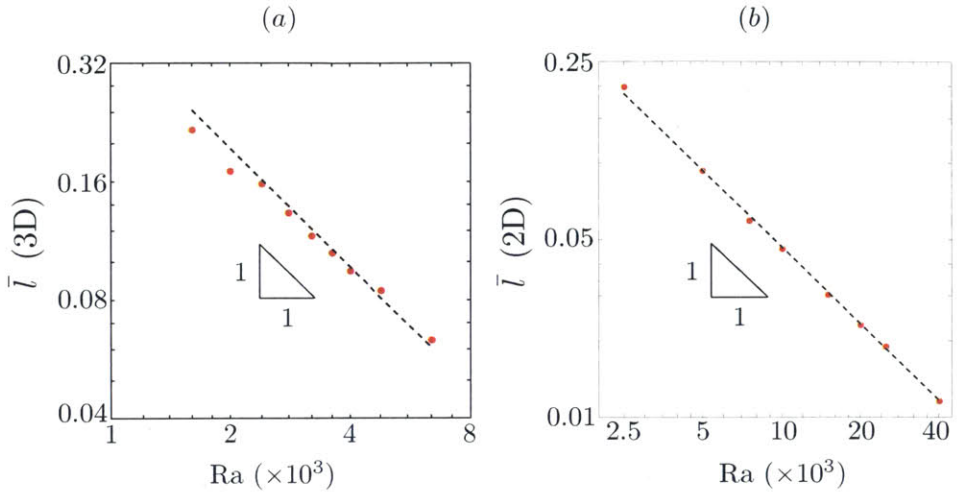

Figure 3-8: Characteristic length $\bar{l}$ plotted against Rayleigh number. (a) 3D simulations; (b) 2D simulations. This characteristic length scale exhibits a power-law dependence with Rayleigh number $\bar{l} \sim \mathrm{Ra}^{-1}$.

section 2(b), although finite-size effects prevent achieving the pseudo-steady state for the smaller values of Ra (1600 and 2000). We choose the overall characteristic length, denoted $\bar{l}$, as the time average of l_{cell} during the *nonequilibrium steady state*, taken here as $10 < t < 15$. This average length scale $\bar{l}$ exhibits a power-law dependence with Rayleigh number, with exponent -1 [Fig. 3-8(a)], supporting the scaling relation in Eq. (3.3).

$$l_{\mathrm{cell}} \sim \mathrm{Ra}^{-1} \tag{3.3}$$

We recognize that it would be useful to extend the study of 3D convective mixing to higher Rayleigh numbers. However, the computational cost would be significant. Instead, we confirm the proposed scaling $\bar{l} \sim \mathrm{Ra}^{-1}$ with 2D simulations, where it is computationally tractable to perform simulations with Ra=40,000. In 2D, the domain is the unit square (1×1), N_{fing} is the number of finger roots in the boundary layer [Fig. 3-5(c)], and the characteristic length is the average finger root spacing: $l_{\mathrm{cell}} = 1/N_{\mathrm{fing}}$. We use a robust peak-finding tool [40] to identify the number of finger roots, which are the peaks in a 1D concentration signal [Fig. 3-5(d)] taken near the boundary [Fig. 3-5(c)]. In Fig. 3-8(b), we plot the time-averaged 2D characteristic

length $\bar{l}$ with Ra in log–log scale, and again observe the same -1 exponent. This strongly suggests that the scaling relation $l_{\text{cell}} \sim \text{Ra}^{-1}$ is universal, both in 2D and 3D, in the regime of large Rayleigh numbers.

Chapter 4

Flow structure and pattern forming mechanisms

4.1 Rayleigh-Bénard convection and linear stability analysis

The hexagonal-like cellular convection pattern was first observed by Henri Bénard in 1900 in a thermal convection experiment [2]. The experiment setup uses a layer of fluid between two parallel plates; the height of the layer is small compared to the horizontal dimension. Initially, the temperatures of the top and bottom plates are the same and the fluid temperature (T) is uniform and same as the surroundings. Then the bottom plate is heated and kept at a constant temperature $T+\Delta T$. At this point, the temperature, and the density and pressure with it, will behave diffusively between the top and bottom plate, resulting in a uniform linear gradient in the field. Any natural imperfections (noise) will then propagate through the established convection field and create Bénard convection cells in the vertical direction (Fig. 4-1). At steady state, one can trace the flow structure in a horizontal plane using a passive tracer and observe hexagonal cellular structures (Fig. 4-2).

Lord Rayleigh was the first to successfully analyze the Bénard cells [28], thus people commonly refer to this problem as Rayleigh-Bénard convection. This fluid

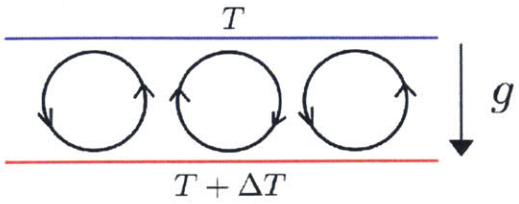

Figure 4-1: A simplified diagram of the Bénard experiment and illustration of the convection cells in vertical direction.

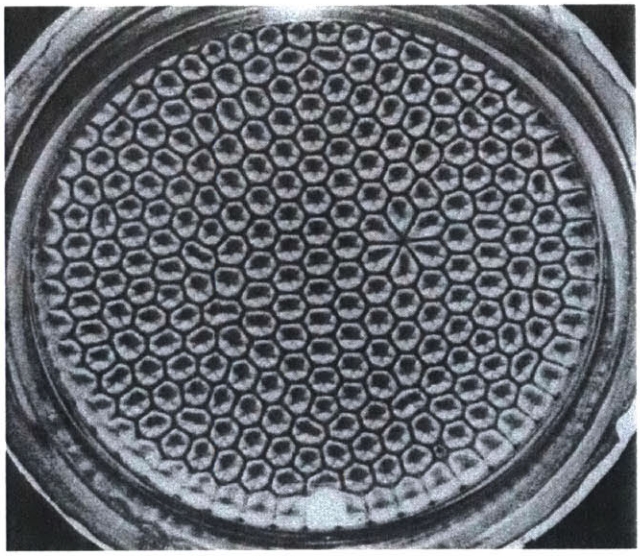

Figure 4-2: Image from [17]. The following captions are from [38]: "Imperfections in a hexagonal Bénard convection pattern. The hexagonal pattern of cells typical of convective instability driven primarily by surface tension is seen to accommodate itself to a circular boundary. Aluminum powder shows the flow in a thin layer of silicone oil of kinematic viscosity 0.5 cm^2/s on a uniformly heated copper plate. A tiny dent in the plate causes the imperfection at the left, forming diamond-shaped cells. This shows how sensitive the pattern is to small irregularities."

mechanics problem has been well studied, including the analytical solution to the hexagonal pattern [5, 3]; see [4] for a comprehensive summary and extended study on the pattern forming process and hexagonal structure in Rayleigh-Bénard convection.

The underlying mechanism of instability in convective mixing is similar to that of the Rayleigh-Bénard convection: in both cases, changes in a scalar field (CO_2 concentration or temperature) lead to changes in density of the fluid and thus create an unstable configuration where a dense fluid sits atop a lighter fluid. On the other hand, with much resemblance to foam dynamics, the hexagonal cellular pattern in convective mixing exhibits more time dynamics and shape irregularities [Fig.3-3 (a)] compared to the classical stationary Rayleigh Bénard pattern (Fig.4-2). Nevertheless, the pattern forming analysis on Rayleigh-Bénard problem [5, 3, 4] should still provide some fundamental understandings of the pseudo-hexagonal cells in dissolution convective mixing.

In the following, we first conduct a linear stability analysis to predict the critical onset Rayleigh number for instability in 3D convective mixing. Then as an extension to the stability problem, we briefly describe the work by Christopherson [5], Bisshopp [3] and Chandrasekhar [4] on the analytical study of hexagonal cell patterns in the Bénard problem. Finally, we compare the velocity field from 3D simulations with the analytical solution and find good agreement between simulated and predicted flow structures.

4.2 Linear stability analysis

We start by revisiting the convective mixing system in dimensionless form [Eq.(2.5)-(2.7)]

$$\nabla \cdot \mathbf{u} = 0, \tag{2.5}$$

$$\mathbf{u} = -(\nabla P' - C\hat{\mathbf{z}}), \tag{2.6}$$

$$\frac{\partial C}{\partial t} = -\mathbf{u} \cdot \nabla C + \frac{1}{\mathrm{Ra}} \nabla^2 C, \tag{2.7}$$

Taking the curl of Eq.(2.6):

$$\begin{aligned}\nabla \times \mathbf{u} &= -(\nabla \times \nabla P' - \nabla \times (C\hat{\mathbf{z}})) \\ &= \frac{\partial C}{\partial y}\mathbf{i} - \frac{\partial C}{\partial x}\mathbf{j}\end{aligned}$$

Taking the curl again and using the identity: $\nabla \times (\nabla \times \mathbf{u}) = \nabla(\nabla \cdot \mathbf{u}) - \nabla^2\mathbf{u}$, we obtain:

$$\begin{aligned}\nabla \times (\nabla \times \mathbf{u}) &= \nabla \times (\frac{\partial C}{\partial y}\mathbf{i} - \frac{\partial C}{\partial x}\mathbf{j}) \\ \nabla(\nabla \cdot \mathbf{u}) - \nabla^2\mathbf{u} &= \frac{\partial^2 C}{\partial x \partial z}\mathbf{i} + \frac{\partial^2 C}{\partial y \partial z}\mathbf{j} - \left(\frac{\partial^2 C}{\partial x^2} + \frac{\partial^2 C}{\partial y^2}\right)\mathbf{k} \\ -(\Delta u\mathbf{i} + \Delta v\mathbf{j} + \Delta w\mathbf{k}) &= \frac{\partial^2 C}{\partial x \partial z}\mathbf{i} + \frac{\partial^2 C}{\partial y \partial z}\mathbf{j} - \left(\frac{\partial^2 C}{\partial x^2} + \frac{\partial^2 C}{\partial y^2}\right)\mathbf{k} \text{ [use Eq.(2.5)]}\end{aligned}$$

Taking only the z component of the above relation:

$$\frac{\partial^2 w}{\partial x^2} + \frac{\partial^2 w}{\partial y^2} + \frac{\partial^2 w}{\partial z^2} = \frac{\partial^2 C}{\partial x^2} + \frac{\partial^2 C}{\partial y^2}$$

or:

$$\nabla^2 w = \nabla^2 C - \frac{\partial^2 C}{\partial z^2} \tag{4.1}$$

Now we decompose the stream-wise velocity w and concentration field C into a base state and a transient state:

$$\begin{aligned}w(x, y, z, t) &= w_0(z, t) + \hat{w}(z)\exp(ilx + imy - i\omega t) = w_0 + \widetilde{w} \\ C(x, y, z, t) &= C_0(z, t) + \hat{C}(z)\exp(ilx + imy - i\omega t) = C_0 + \widetilde{C}\end{aligned}$$

Similar perturbations are introduced to u, v: $u = u_0 + \widetilde{u}$, $v = v_0 + \widetilde{v}$. The base velocity u_0, v_0, w_0 are zero here and the base concentration C_0 satisfies Eq.(2.6) and (2.7) with $\mathbf{u} = 0$ and $\partial/\partial(x, y) = \partial^2/\partial(x^2, y^2) = 0$:

$$\frac{\partial C_0}{\partial t} = \frac{1}{\mathrm{Ra}}\nabla^2 C_0 = \frac{1}{\mathrm{Ra}}\frac{\partial^2 C_0}{\partial z^2} \tag{4.2}$$

The general solution to the base state problem [Eq.(4.2)] is [29]:

$$C_0(z,t) = 1 - \frac{4}{\pi}\sum_{n=1}^{\infty}\frac{1}{2n-1}\sin((n-1/2)\pi z)\exp(-(n-1/2)^2\pi^2 t/\mathrm{Ra}) \tag{4.3}$$

The perturbation variables $\widetilde{w}$ and $\widetilde{C}$ are decomposed into eigenfunctions $\hat{w}$ and $\hat{C}$, which depend on the streamwise coordinate, and normal modes in the x and y-direction and time domain with wavenumbers being l, m respectively and time frequency being ω. The linearized perturbation equation derived from Eq.(4.1) and (2.7) then becomes:

$$(D^2-a^2)\widetilde{w} = \frac{\partial^2 C_0}{\partial z^2} + (D^2-a^2)\widetilde{C} - \frac{\partial^2 C_0}{\partial z^2} - D^2\widetilde{C}$$

$$\frac{\partial C_0}{\partial t} + (-i\omega)\widetilde{C} = -\left(\widetilde{u}\frac{\partial \widetilde{C}}{\partial x} + \widetilde{v}\frac{\partial \widetilde{C}}{\partial y} + \widetilde{w}(\frac{\partial C_0}{\partial z} + \frac{\partial \widetilde{C}}{\partial x})\right) + \frac{1}{\mathrm{Ra}}\left(\frac{\partial^2 C_0}{\partial z^2} + (D^2-a^2)\widetilde{C}\right)$$

Here $D = \frac{\partial}{\partial z}$ and $a^2 = l^2 + m^2$. ω here is the time frequency; following the principle of exchange of stabilities [22] one can determine that ω is purely imaginary. When $\omega < 0$, the solution is stable and will decay to zero; when $\omega > 0$ the solution is unstable. Marginal stability occurs when $\omega = 0$. We consider here the situation of marginal stability: $\omega = 0$. After linearization by eliminating second order perturbations and some simplifications:

$$(D^2-a^2)\widetilde{w} = -a^2\widetilde{C} \tag{4.4}$$

$$\frac{\partial C_0}{\partial t} = -\widetilde{w}\frac{\partial C_0}{\partial z} + \frac{1}{\mathrm{Ra}}\left(\frac{\partial^2 C_0}{\partial z^2} + (D^2-a^2)\widetilde{C}\right) \tag{4.5}$$

Since C_0 satisfies the base state problem described by Eq.(4.2), we can further simplify Eq.(4.5):

$$\widetilde{w}\frac{\partial C_0}{\partial z} = \frac{1}{\mathrm{Ra}}(D^2-a^2)\widetilde{C} \tag{4.6}$$

Eliminating $\widetilde{C}$ using Eq.(4.4) and (4.6):

$$(D^2-a^2)^2\widetilde{w} = a^2\mathrm{Ra}\frac{\partial C_0}{\partial z}\widetilde{w}, \tag{4.7}$$

where $\widetilde{w}$ is subject to:

$$\widetilde{w} = 0, \;\; D^2\widetilde{w} = 0 \text{ for } z = 0, 1 \tag{4.8}$$

Expanding Eq.(4.7):

$$D^4\widetilde{w} - 2a^2D^2\widetilde{w} + a^4\widetilde{w} = a^2\mathrm{Ra}\frac{\partial C_0}{\partial z}\widetilde{w} \tag{4.9}$$

Applying Eq.(4.8), it is clear that $D^4\widetilde{w} = 0$ on $z = 0, 1$. Differentiating Eq.(4.9) twice in z, we obtain:

$$D^6\widetilde{w} - 2a^2D^4\widetilde{w} + a^4D^2\widetilde{w} = a^2\mathrm{Ra}\left(\frac{\partial^3 C_0}{\partial z^3}\widetilde{w} + \frac{\partial C_0}{\partial z}D^2\widetilde{w}\right)$$

Here we assume that C_0 is n^{th} differentiable: $\partial^n C_0/\partial z^n$ exists, which is a reasonable assumption derived from Eq.(4.3). Analogously we get $D^6\widetilde{w} = 0$ on $z = 0, 1$. Repeating this exercise, we conclude that

$$D^{2n}\widetilde{w} = 0, \quad n = 0, 1, 2, \ldots \quad \text{for } z = 0, 1.$$

This indicates that a solution for $\widetilde{w}$ is of the form:

$$\widetilde{w} = \sin(j\pi z)$$

We apply the above solution to Eq. (4.7) to obtain that:

$$\mathrm{Ra}\frac{\partial C_0}{\partial z} = \frac{(j^2\pi^2 + a^2)^2}{a^2}, \quad \text{for } j = 1, 2, 3...$$

The right hand side approaches ∞ as a^2 goes to 0 or ∞, and reaches minimum when $\partial/\partial a^2 = 0$: $a^2 = \pi^2$. In other words,

$$\mathrm{Ra}\frac{\partial C_0}{\partial z} \geq 4\pi^2$$

We can estimate the bounds for $\dfrac{\partial C_0}{\partial z}$ from Eq.(4.3), assuming that $\dfrac{\partial C_0}{\partial z} \approx 1$, the

critical number is then:

$$\mathrm{Ra}_c = 4\pi^2$$

The system becomes unstable when Ra> Ra_c and behaves in a stable diffusive manner when Ra< Ra_c.

4.3 Analytical and simulated two-dimensional cell patterns

The following is a summary of the work by [5, 3, 4] on stationary hexagonal patterns in Rayleigh-Bénard convection. At steady-state of this problem, the horizontal dependence of the fluid motions and temperature perturbations is generally assumed to be separable. In particular, one can assume:

$$w(x,y,z) = W(z)\Phi(x,y)$$
$$T(x,y,z) = \beta z + \Theta(z)\Phi(x,y), \qquad \beta \equiv \Delta T/d$$

where d is the distance between top and bottom plates. By solving the stability problem posed by the above, one find that Φ satisfies the equation:

$$\left(\frac{\partial^2}{\partial x^2} + \frac{\partial^2}{\partial y^2}\right)\Phi = -a^2\Phi,$$

where a is the horizontal wavenumber as defined in Sec. 4.2. Christopherson [5] first discovered the solution to the above problem for hexagonal pattern:

$$w = \frac{1}{3}W(z)\{2\cos\frac{2\pi}{L\sqrt{3}}x\cos\frac{2\pi}{3L}y + \cos\frac{4\pi}{3L}y\}$$

where $L = \dfrac{2\pi}{a}$ is a constant. By performing a change of variables:

$$x = \omega\cos\theta, \qquad y = \omega\sin\theta,$$

one can discover the basic hexagonal symmetry from the updated solution rewritten in terms of ω, θ:

$$w = \frac{1}{3}W(z)\left\{\cos[\frac{4\pi\omega}{3L}\sin(\theta+\frac{\pi}{3})] + \cos[\frac{4\pi\omega}{3L}\sin(\theta+\frac{2\pi}{3})] + \cos[\frac{4\pi\omega}{3L}\sin(\theta)]\right\}$$

From this it is apparent that:

$$w(\omega,\theta) = w(\omega,\theta+\frac{\pi}{3}),$$

indicating that the solution is invariant for rotation by $\frac{\pi}{3} = 60°$ about the origin. In addition, the solution also exhibits periodicity in the x and y directions:

$$w(x+nL\sqrt{3}, y+3mL) \equiv w(x,y)$$

One can also study the solution along characteristic lines and points. For example, at the origin, $x = y = 0$, the solution is:

$$w(0) = W(z). \tag{4.10}$$

Along the three pairs of lines (forming a hexagon on the $x-y$ plane):

$$y = \pm\frac{3}{4}L, \quad x\sqrt{3}+y = \pm\frac{3}{2}L, \quad x\sqrt{3}-y = \pm\frac{3}{2}L,$$

the solution is:

$$w = -\frac{1}{3}W(z) \tag{4.11}$$

At the six points (six vertices of another hexagon):

$$\left(\frac{\sqrt{3}}{2}L, \pm\frac{1}{2}L\right), (0, \pm L), \left(-\frac{\sqrt{3}}{2}L, \pm\frac{1}{2}L\right),$$

the solution is:

$$w = -\frac{1}{2}W(z) \tag{4.12}$$

One can also derive the horizontal velocities with the following relations:

$$u = \frac{1}{a^2}\frac{\partial^2 w}{\partial x \partial z}$$
$$v = \frac{1}{a^2}\frac{\partial^2 w}{\partial y \partial z},$$

and obtain that $u = v = 0$ along the hexagon boundaries.

We compare the above analysis with the simulated velocity field in convective mixing, and find good agreement. Fig. 4-3 shows a simulation with Ra=3200 and snapshots of the velocity fields at $t = 12$. Notice that the horizontal velocity is indeed zero along the cell boundaries (Fig.4-3, 2nd frame). Furthermore, the vertical velocity (w) is upward (positive) and large in the center of the cells (Fig.4-3, 4th frame; Eq.4.10); w is downward (negative) along the cell boundaries and is larger on cell vertices than the boundaries (Fig.4-3, 3rd frame; Eq.4.11 and 4.12)

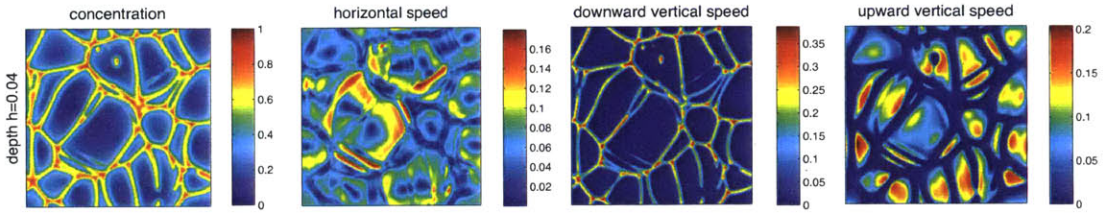

Figure 4-3: For a simulation of Ra=3200, snapshots at $t = 12$ of horizontal slices at $z = 0.04$. From left to right: concentration field, flow speed in x-y plane (horizontal speed), flow speed in positive z-direction (downward) and flow speed in negative z-direction (upward).

Chapter 5

Conclusion

In this thesis, we have studied the pattern-formation aspects of convective mixing in porous media, a phenomenon of relevance in CO_2 sequestration in deep saline aquifers. We have analyzed the process by means of high-resolution simulations in a simplified geometry. Our key observation is the emergence of a cellular network structure in the diffusive boundary layer at the top boundary. Theoretical arguments and statistical analysis of the evolving pattern allowed us to discern the fundamental scaling properties of this pattern in space and time. In particular, we have identified a period of coarsening followed by a nonequilibrium steady state, and explained the detailed mechanisms—cell growth and cell division—responsible for this behavior.

We investigate the onset of instability via a linear stability analysis of the 3D problem. Through the analysis, we determine the critical Rayleigh number to be Ra= $4\pi^2$, consistent with previous analysis by [14] on a similar problem regarding thermal convection. Seeking insights into the pattern forming mechanism through earlier work using perturbation theory, we reviewed briefly the analysis done by [5, 3, 4] on the hexagonal cellular patterns in convection. We then compare the predicted velocity field from the analytical stability solution to observations from simulation and find that they agree well: no horizontal flow occurs along the hexagonal cell boundaries; vertical flow is upward and largest in cell centers; vertical flow is downward on cell boundaries and is larger on cell vertices than on cell edges.

Bibliography

[1] S. Backhaus, K. Turitsyn, and R. E. Ecke. Convective instability and mass transport of diffusion layers in a Hele-Shaw geometry. *Phys. Rev. Lett.*, 106(10):104501, 2011.

[2] H. Bénard. Les tourbillons cellulaires dans une nappe liquide. *Rev. Gen. Sci. pures et appl.*, 11:1261–1271 & 1309 –1328, 1900.

[3] F. E. Bisshopp. On two-dimensional cell patterns. *J. Math. Analysis and Applications.*, 1:373–85, 1960.

[4] S. Chandrasekhar. *Hydrodynamics and Hydromagnetic Stability.* Dover Books on Physics Series. Dover Publications, 1961.

[5] D.G. Christopherson. Note on the vibration of membranes. *Quart. J. of Math.*, 11:63–65, 1940.

[6] J. Ennis-King and L. Paterson. Role of convective mixing in the long-term storage of carbon dioxide in deep saline formations. *Soc. Pet. Eng. J.*, 10(3):349–356, September 2005.

[7] J. Ennis-King, I. Preston, and L. Paterson. Onset of convection in anisotropic porous media subject to a rapid change in boundary conditions. *Phys. Fluids*, 17(8):084107, 2005.

[8] H. Hassanzadeh, M. Pooladi-Darvish, and D. W. Keith. Scaling behavior of convective mixing, with application to geological storage of CO_2. *AIChE J.*, 53(5):1121–1131, 2007.

[9] A. Henderson. Paraview guide, a parallel visualization application. *Kitware Inc.*, 2007.

[10] D. R. Hewitt, J. A. Neufeld, and J. R. Lister. Convective shutdown in a porous medium at high Rayleigh number. *J. Fluid Mech.*, 719:551–586, 2013.

[11] J. J. Hidalgo and J. Carrera. Effect of dispersion on the onset of convection during CO_2 sequestration. *J. Fluid Mech.*, 640:441–452, 2009.

[12] J. J. Hidalgo, J. Fe, L. Cueto-Felgueroso, and R. Juanes. Scaling of convective mixing in porous media. *Phys. Rev. Lett.*, 109(26):264503, 2012.

[13] C. W. Horton and F. T. Rogers. Convection Currents in a Porous Medium. *Journal of Applied Physics*, 16(6):367, 1945.

[14] C. W. Horton and F. T. Rogers. Convection currents in a porous medium. *J. of Applied Phys.*, 16:367–370, 1945.

[15] IPCC. *Special Report on Carbon Dioxide Capture and Storage,* B. Metz et al. (eds.). Cambridge University Press, 2005.

[16] T. J. Kneafsey and K. Pruess. Laboratory flow experiments for visualizing carbon dioxide-induced, density-driven brine convection. *Transp. Porous Media*, 82:123–139, 2010.

[17] E. L. Koschmieder. Bénard convection. *Adv. Chem. Phys.*, 26:177–212, 1974.

[18] K. S. Lackner. A guide to CO_2 sequestration. *Science*, 300(5626):1677–1678, 2003.

[19] Sanjiva K. Lele. Compact finite difference schemes with spectral-like resolution. *J. Comput. Phys.*, 103(1):16–42, 1992.

[20] E. Lindeberg and D. Wessel-Berg. Vertical convection in an aquifer column under a gas cap of CO_2. *Energy Conv. Manag.*, 38:S229–S234, 1997.

[21] Matlab. Image processing toolbox. http://www.mathworks.com/products/image/#thd1, 2012.

[22] C. C. Mei. Horton-Rogers-Lapwood instability in a porous layer. Lecture notes for Advanced Environmental Fluid Mechanics, MIT, 2002.

[23] J. A. Neufeld, M. A. Hesse, A. Riaz, M. A. Hallworth, H. A. Tchelepi, and H. E. Huppert. Convective dissolution of carbon dioxide in saline aquifers. *Geophys. Res. Lett.*, 37:L22404, 2010.

[24] D. A. Nield and A. Bejan. *Convection in Porous Media.* Springer, New York, third edition, 2006.

[25] F. M. Orr, Jr. Onshore geologic storage of CO_2. *Science*, 325:1656–1658, 2009.

[26] G. S. H. Pau, J. B. Bell, K. Pruess, A. S. Almgren, M. J. Lijewski, and K. Zhang. High-resolution simulation and characterization of density-driven flow in CO_2 storage in saline aquifers. *Adv. Water Resour.*, 33(4):443–455, 2010.

[27] S. Rapaka, S. Chen, R. J. Pawar, P. H. Stauffer, and D. Zhang. Non-modal growth of perturbations in density-driven convection in porous media. *J. Fluid Mech.*, 609:285–303, 2008.

[28] Lord Rayleigh. On the convective currents in a horizontal layer of fluid when the higher temperature is on the under side. *Phil. Mag.*, 32:529546, 1916.

[29] A. Riaz, M. Hesse, H. A. Tchelepi, and F. M. Orr, Jr. Onset of convection in a gravitationally unstable, diffusive boundary layer in porous media. *J. Fluid Mech.*, 548:87–111, 2006.

[30] M. Ruith and E. Meiburg. Miscible rectilinear displacements with gravity override. Part 1. Homogeneous porous medium. *J. Fluid Mech.*, 420:225–257, 2000.

[31] C.A. Schneider, W.S. Rasband, and K. W. Eliceiri. NIH Image to ImageJ: 25 years of image analysis. *Nat. Methods*, (9):671–675, 2012.

[32] A. Slim. Solutal-convection regimes in a two-dimensional porous medium. *J. Fluid Mech.*, 741:461–491, 2014.

[33] A. Slim, M. M. Bandi, J. C. Miller, and L. Mahadevan. Dissolution-driven convection in a Hele-Shaw cell. *Phys. Fluids*, 25:024101, 2013.

[34] A. Slim and T. S. Ramakrishnan. Onset and cessation of time-dependent, dissolution-driven convection in porous media. *Phys. Fluids*, 22(12):124103, 2010.

[35] P. N. Swarztrauber. The methods of cyclic reduction, Fourier analysis, and the FACR algorithm for the discrete solution of Poissons equation on a rectangle. *SIAM Rev.*, 19:490–501, 1977.

[36] M. L. Szulczewski, C. W. MacMinn, H. J. Herzog, and R. Juanes. The lifetime of carbon capture and storage as a climate-change mitigation technology. *Proc. Natl. Acad. Sci. U.S.A.*, 109(14):5185–5189, 2012.

[37] L.N. Trefethen. *Spectral Methods in MATLAB.* SIAM, 2000.

[38] M. Van Dyke. *An Album of Fluid Motion.* Parabolic Press, 1982.

[39] G. J. Weir, S. P. White, and W. M. Kissling. Reservoir storage and containment of greenhouse gases. *Transp. Porous Media*, 23(1):37–60, 1996.

[40] N. Yoder. Peakfinder. MATLAB Central File Exchange, http://www.mathworks.com/matlabcentral/fileexchange/25500-peakfinder, 2009.